ADVANCED MATERIALS
www.advmat.de

Conductive Metal–Organic Framework Nanosheets Constructed Hierarchical Water Transport Biological Channel for High-Performance Interfacial Seawater Evaporation

Yongqiang Qian, Guanfeng Xue, Luzhuo Chen, Gang Xu, and Guan-E Wang**

Solar interfacial water evaporation shows great potential to address the global freshwater scarcity. Water evaporation being inherently energy intensive, Joule-heating assisted solar evaporation for addressing insufficient vapor under natural conditions is an ideal strategy. However, the simultaneous optimization of low evaporation enthalpy, high photothermal conversion, and excellent Joule-heating steam generation within a single material remain a rare achievement. Herein, inspired by the biological channel structures, a large-area film with hierarchical macro/microporous structures is elaborately designed by stacking the nanosheet of a conductive metal–organic framework (MOF), $Ni_3(HITP)_2$, on a paper substrate. By combining the above three features in one material, the water evaporation enthalpy reduces from 2455 J g^{-1} to 1676 J g^{-1}, and the photothermal conversion efficiency increases from 13.75% to 96.25%. Benefiting from the synergistic photothermal and Joule-heating effects, the evaporation rate achieves 2.60 kg m^{-2} h^{-1} under one sun plus input electrical power of 4 W, surpassing the thermodynamic limit and marking the highest reported value in MOF-based evaporators. Moreover, $Ni_3(HITP)_2$-paper exhibits excellent long-term stability in simulated seawater, where no salt crystallization and evaporation rate degradation are observed. This design strategy for nanosheet films with hierarchical macro/microporous channels provides inspiration for electronics, biological devices, and energy applications.

1. Introduction

Freshwater scarcity has emerged a pressing global issue due to population growth, urbanization, and climate change.[1] To address the water crisis, desalination and wastewater purification through solar-driven water evaporation have gained prominence as significant and sustainable solutions.[2,3] Recently, interfacial water evaporation, which utilizes solar absorbers to heat the surface of bulk water for efficient steam generation, has attracted significant attention from researchers.[4–8] The evaporation rate serves as a pivotal metric for evaluating the performance of solar steam generation devices. Nevertheless, due to the intrinsic energy limitations of water evaporation, the theoretical evaporation rate of an evaporator typically remains below 1.47 kg m^{-2} h^{-1} (the thermodynamic evaporation limit) under one sun (1 kW m^{-2}).[4,8] This low evaporation rate is inadequate for industries that require fast, energy-efficient, and cost-effective evaporation processes such as distillation, purification, sterilization, and more.[5]

Y. Qian, G. Xue, L. Chen
Fujian Provincial Key Laboratory of Quantum Manipulation and New Energy Materials
College of Physics and Energy
Fujian Normal University
Fuzhou 350117, P. R. China
E-mail: ChenLZ@fjnu.edu.cn

Y. Qian, G. Xue, L. Chen
Fujian Provincial Collaborative Innovation Center for Advanced High-Field Superconducting Materials and Engineering
Fuzhou 350117, P. R. China

G. Xu, G.-E Wang
State Key Laboratory of Structural Chemistry
Fujian Institute of Research on the Structure of Matter
Chinese Academy of Sciences (CAS)
Fuzhou 350117, P. R. China
E-mail: gewang@fjirsm.ac.cn

G. Xu
Fujian Science & Technology Innovation Laboratory for Optoelectronic Information of China
Fuzhou 350108, P. R. China

The ORCID identification number(s) for the author(s) of this article can be found under https://doi.org/10.1002/adma.202310795

DOI: 10.1002/adma.202310795

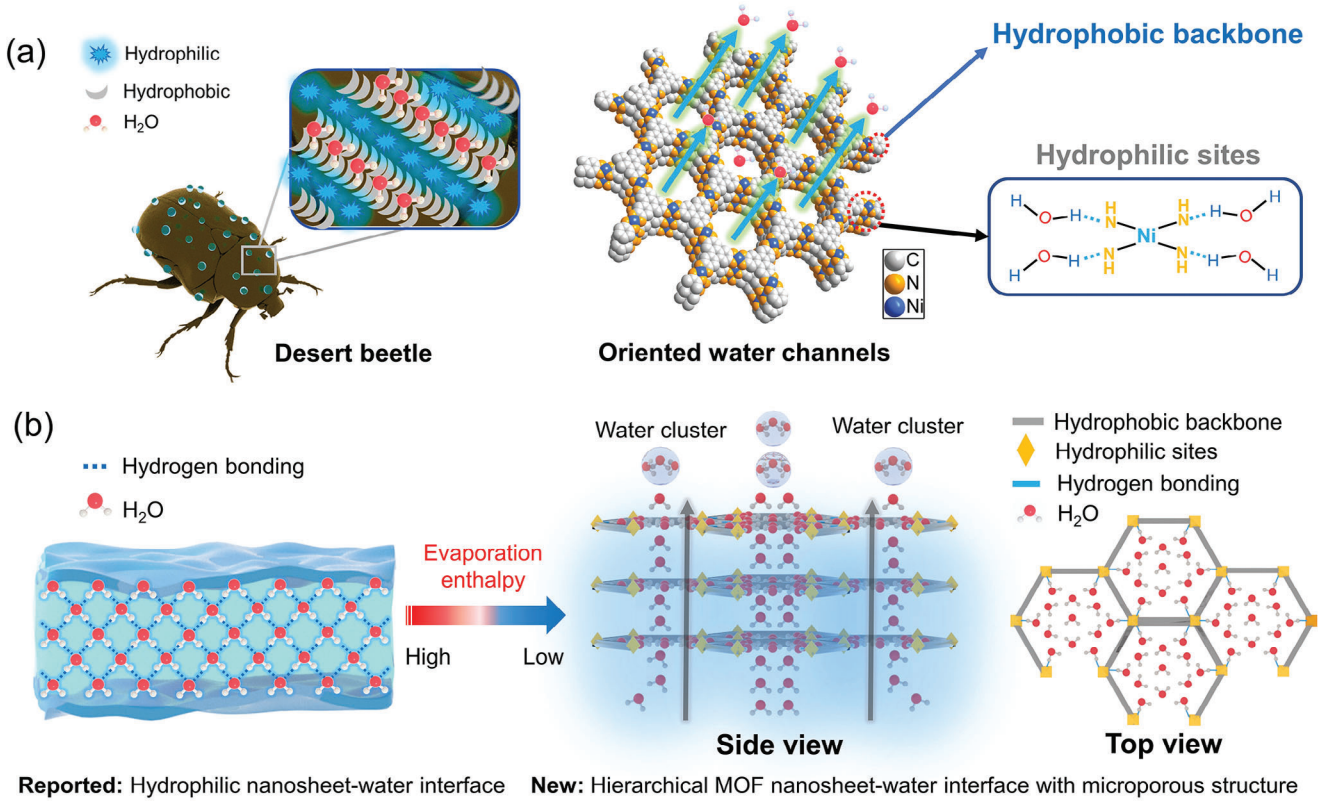

Scheme 1. a) Biological hydrophilic and hydrophobic structures in desert beetle and oriented water channels in hierarchical MOF with hydrophobic backbone-hydrophilic sites. b) Traditional hydrophilic nanosheet–water interface and new hierarchical MOF nanosheet–water interface with microporous structure.

In addition, solar steam generators often confront efficiency challenges at night or rainy days due to insufficient sunlight. The introduction of electrical stimulation in a material via an additional electrical device (e.g., a direct current power supply), which employs the heat generated by the passage of an electric current through the material (the Joule-heating process), can be used to assist in solar water evaporation. Therefore, the combination of a photothermal and Joule-heating process can significantly address the issue of insufficient energy for solar water evaporation systems as well as the dependence on the duration of the illumination; and thus, offer a potential solution to these challenges.[6,7] However, achieving simultaneous optimization of low evaporation enthalpy, high photothermal conversion efficiency, and excellent electrical performance within a single material remains a rare accomplishment. Consequently, the development of an efficient steam generator capable of functioning under all-weather conditions represents an urgent and paramount pursuit.

Nanosheet structures, exemplified by inorganic nanosheets (arrays), represent an ideal structural configuration for interfacial water evaporation.[9–12] Devices featuring nanosheet morphology boast an expansive surface area, facilitating the creation of intricate pathways to minimize heat dissipation.[9] Further, they enable multiple reflections of light on the surface of the devices, effectively enhancing solar energy harvesting and thereby improving photothermal conversion efficiency.[10] Consequently, nanosheet structures represent an especially advantageous morphology for photothermal conversion materials. For example, materials such as MXene and graphene,[13,14] which typically exhibit nanosheet morphology, feature excellent photothermal conversion properties. However, the low resistivity of these materials is unfavorable for Joule-heating conversion. In addition, the high thermal conductivity of these materials makes it easy for heat to diffuse into the surrounding medium, which is not conducive to water evaporation at the interface, thereby resulting in reduced heat-to-vapor conversion efficiency.[15] The development of unique water transport channels in nanosheet materials can be an effective solution to these issues. Nevertheless, the practical realization of water transport channels on these materials remains a formidable undertaking.

In nature, organisms such as desert beetle, cactus, and desert grass possess both hydrophilic and hydrophobic structures in their bodies that enable them to efficiently collect and transfer water in extremely arid environments.[16,17] The hydrophilic structures are used for efficient capture of vapor; while, the hydrophobic structures are used for rapid transportation of liquid droplets. Inspired by biological structures, the inherent nano-pore structures in metal–organic framework (MOF) materials[18–21] make them suitable to act as an ideal material for highly effective interfacial water evaporation (**Scheme 1a**). First, the micropores of MOFs can mimick biological structures to possess a unique channel structure with hydrophilic–hydrophobic binding. Specifically,

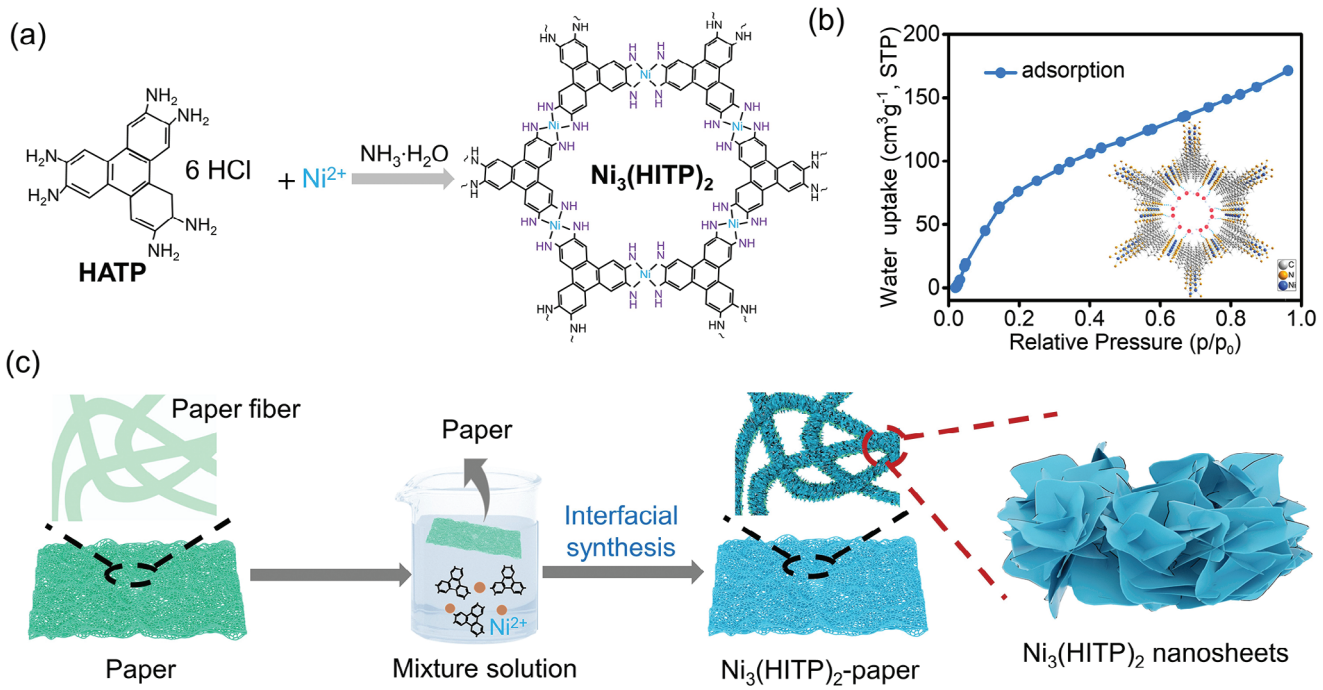

Figure 1. a) General synthetic of $Ni_3(HITP)_2$ MOFs. b) Water uptake isotherm of $Ni_3(HITP)_2$ at room temperature; inset shows the pore channel structures of $Ni_3(HITP)_2$. c) Schematic diagram of the fabrication process of $Ni_3(HITP)_2$-paper composite film by interface-induced growth.

the hydrophobic backbone in the micropores of MOFs serves to reduce the affinity between the channels and water molecules, effectively lowering the energy barrier for water molecule transmission. Conversely, the hydrophilic sites weaken the interactions among water molecules, resulting in a significantly reduced enthalpy of water evaporation (Scheme 1b). Second, the microporous structure in MOFs possesses the capacity to reflect and scatter phonons to depress the thermal conductivity and thus promote heat-to-vapor conversion efficiencies.[22,23] Third, combined with the appropriate electrical conductivity of conductive MOFs,[24] simultaneous Joule-heating assisted evaporation with solar evaporation can be achieved, leading to an improved water evaporation rate. Nevertheless, the fabrication of conductive MOFs nanosheets, particularly their further assembly into a large-area film, and the utilization of the merits of MOF and nanosheet coupling for interfacial water evaporation, have not been reported yet.

Herein, we first report a large-size MOF film constructed with $Ni_3(HITP)_2$ nanosheets, which functions as a high-efficiency water evaporator capable of harnessing both photothermal and Joule-heating interfacial water evaporation, referred to as $Ni_3(HITP)_2$-paper. The $Ni_3(HITP)_2$ is selected due to its unique features derived from our experiments, including ultralow enthalpy of water evaporation (1676 J g^{-1}) owing to the hydrophilic sites and hydrophobic backbone in its channels; large photothermal conversion efficiency (up to 96.25%) due to its exceptionally strong and wide spectral absorption, low thermal conductivity, and light-trapping effect inherent in gaps among its nanosheets; and the moderate resistivity of $Ni_3(HITP)_2$. As a result, the $Ni_3(HITP)_2$-paper evaporator shows an evaporation rate as high as 2.60 kg m^{-2} h^{-1} under light intensity of 1 kW m^{-2} plus input electrical power of 4 W, marking the highest reported value for MOF-based evaporators. Interestingly, $Ni_3(HITP)_2$ nanosheets, possessing a negative charge, enable selective separation of salt ions and water to prevent salt crystallization. With this unusual feature, the $Ni_3(HITP)_2$-paper can keep its high efficiency for a long-term even in seawater.

2. Results and Discussion

The $Ni_3(HITP)_2$ has garnered significant attention due to its distinctive structural characteristics and excellent electrical properties.[22,25–28] This compound exhibits a honeycomb structure featuring long-range ordered 1D channels created by the assembly of square planar coordination metal ions (Ni^{2+}) and π-conjugated ligands (HITP = 2,3,6,7,10,11-hexaiminotriphenylene) (**Figure 1a**).[24,29,30] As a result, the channels are composed of benzene rings and show hydrophobic feature. Meanwhile, the channels are decorated with hydrophilic amine functional groups.[31] Notably, this structure emulates the hydrophilic–hydrophobic interactions present in biological organisms. It effectively mitigates the hydrogen bond interaction between water molecules and the channel walls, facilitating rapid passage of water molecules. This characteristic is substantiated by the water adsorption isotherm of the synthesized $Ni_3(HITP)_2$ at room temperature (Figure 1b). At lower relative pressure (P/P_0 < 0.20), $Ni_3(HITP)_2$ exhibits increased water adsorption due to the abundant hydrophilic sites on the molecular backbone. Conversely, at higher relative pressures (P/P_0 > 0.20), $Ni_3(HITP)_2$ undergoes continuous pore filling without significant changes in the adsorption isotherms. This behavior can be attributed to the higher density of hydrophilic sites lining the pore walls of $Ni_3(HITP)_2$, enabling water to be adsorbed uniformly throughout

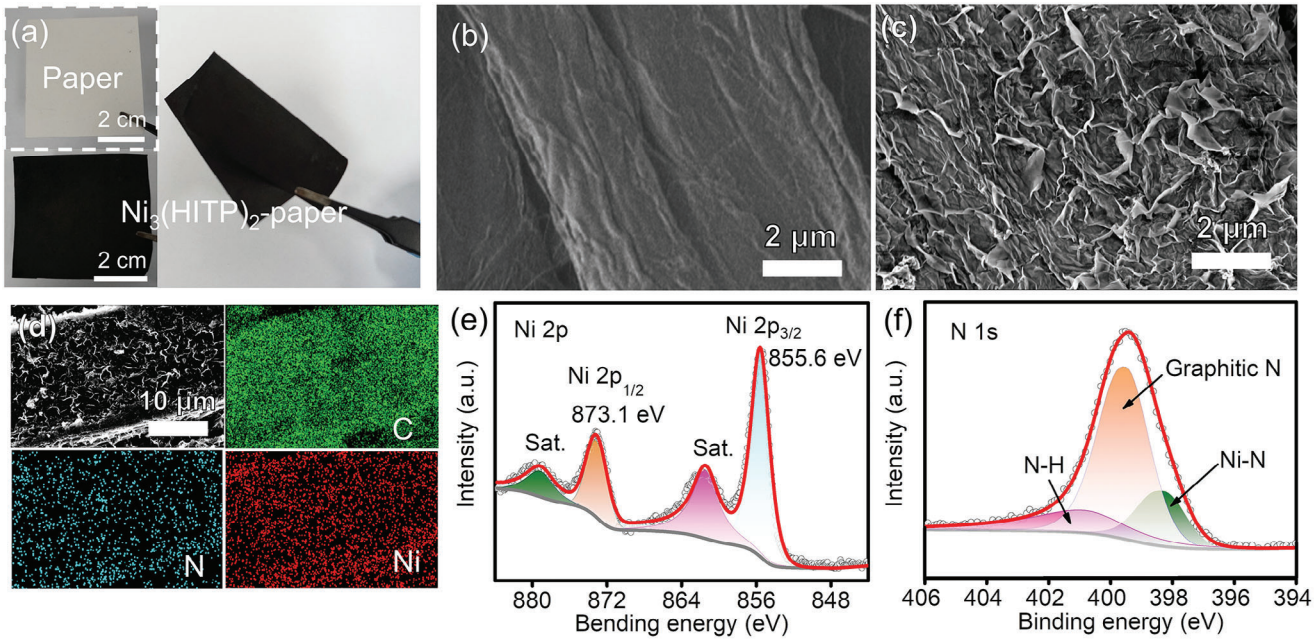

Figure 2. a) Optical photographs of the pristine paper and $Ni_3(HITP)_2$-paper. b) SEM image of the pristine paper. c) SEM image of the $Ni_3(HITP)_2$-paper. d) SEM image of the $Ni_3(HITP)_2$-paper and its corresponding elemental mappings for C, N, and Ni. e) High-resolution XPS core spectra corresponding to Ni 2p and f) N 1s of $Ni_3(HITP)_2$.

the pores.[32] Ultimately, the maximum water uptake achieved by $Ni_3(HITP)_2$ is 171.4 $cm^3\ g^{-1}$.

Oriented 2D nanosheet films exhibit significant potential for photothermal conversion.[9–11,33] However, achieving controlled growth of MOF nanosheets on flexible substrates has proven to be a formidable task due to the inherently weak interactions between rigid MOFs and pliable substrates. We have successfully addressed the issue by modifying the alkalinity of the reaction solution, thereby facilitating the preparation of $Ni_3(HITP)_2$ nanosheets on paper through interface-induced growth. For the formation of nanosheet structures, we hypothesize that a relatively alkaline environment facilitates the rapid amination of ligand molecules, making it easier for them to coordinate with metal ions and promoting the expansion of the material along the layer direction. Consequently, this leads to the material adopting a nanosheet-like structure in its morphology. A schematic diagram of the fabrication process is shown in Figure 1c. First, a mixed aqueous solution of HITP (2,3,6,7,10,11-hexamethylenetriphenylene) and nickel (II) chloride hexahydrate was continuously stirred at 65 °C. The paper was soaked into the reaction mixture. After that, $NH_3{\bullet}H_2O$ was dropwise added to the above mixture. Notably, modulating the amount of $NH_3{\bullet}H_2O$ to control the pH of the reaction mixture between 8 and 9, the growth of $Ni_3(HITP)_2$ nanosheets on fibers was successfully achieved. To attain larger nanosheets, we employed a secondary growth process to ensure uniform coverage of the nanosheets. Afterward, the film was washed repeatedly with ethanol and deionized water, respectively. Finally, the $Ni_3(HITP)_2$-paper composite film was obtained by drying. Detailed preparation process is provided in the Experimental Section. The $Ni_3(HITP)_2$-paper composite film was ultrasonicated and soaked in water for a long period of time. Remarkably, there was no significant shedding of $Ni_3(HITP)_2$ observed during these processes (e.g., ultrasonic and soaking), underscoring the excellent stability of the composite material (Figure S1, Supporting Information).

The optical photographs illustrate a clear comparison between the pristine paper and the synthesized $Ni_3(HITP)_2$-paper (**Figure 2a**). Notably, the $Ni_3(HITP)_2$-paper composite film exhibits a high degree of flexibility as it can be bent without compromising its structural integrity. Scanning electron microscope (SEM) image (Figure S2, Supporting Information; Figure 2b) of the pristine paper shows that it consists of bundles of fibers with varying sizes, intricately interwoven to form a network. Moreover, there are discernible gaps between these fiber bundles. Upon continuous growth of $Ni_3(HITP)_2$, the film retains the structural integrity of the paper fibers. Consequently, the $Ni_3(HITP)_2$-paper still keeps the micrometer-scale macroporous structure of the substrate. The SEM image of the $Ni_3(HITP)_2$ hierarchical structure showcases the complete coverage of paper fibers by oriented $Ni_3(HITP)_2$ nanosheets (Figure 2c). The nanosheets are almost vertically aligned on the substrate and interlace with each other to form a staggered network. Figure 2d shows the SEM image of $Ni_3(HITP)_2$-paper and its corresponding elemental mappings. The uniform distribution of C, N, and Ni in mappings indicates that $Ni_3(HITP)_2$ evenly grows on paper fibers. In addition, the cross-sectional SEM image of the pristine paper reveals that the film possesses a consistent thickness of ≈180 μm; while, the $Ni_3(HITP)_2$-paper maintains a uniform thickness of 190 μm (Figure S3, Supporting Information). The X-ray diffraction (XRD) patterns of $Ni_3(HITP)_2$-paper composite film exhibit the characteristic peaks of $Ni_3(HITP)_2$ at ≈4.6°, 9.4°, 12.5°, 16.5°, and 27.1°, indicative of its typical crystal structure, confirming the successful synthesis of $Ni_3(HITP)_2$ (Figure S4, Supporting Information).[24] Importantly, the N_2

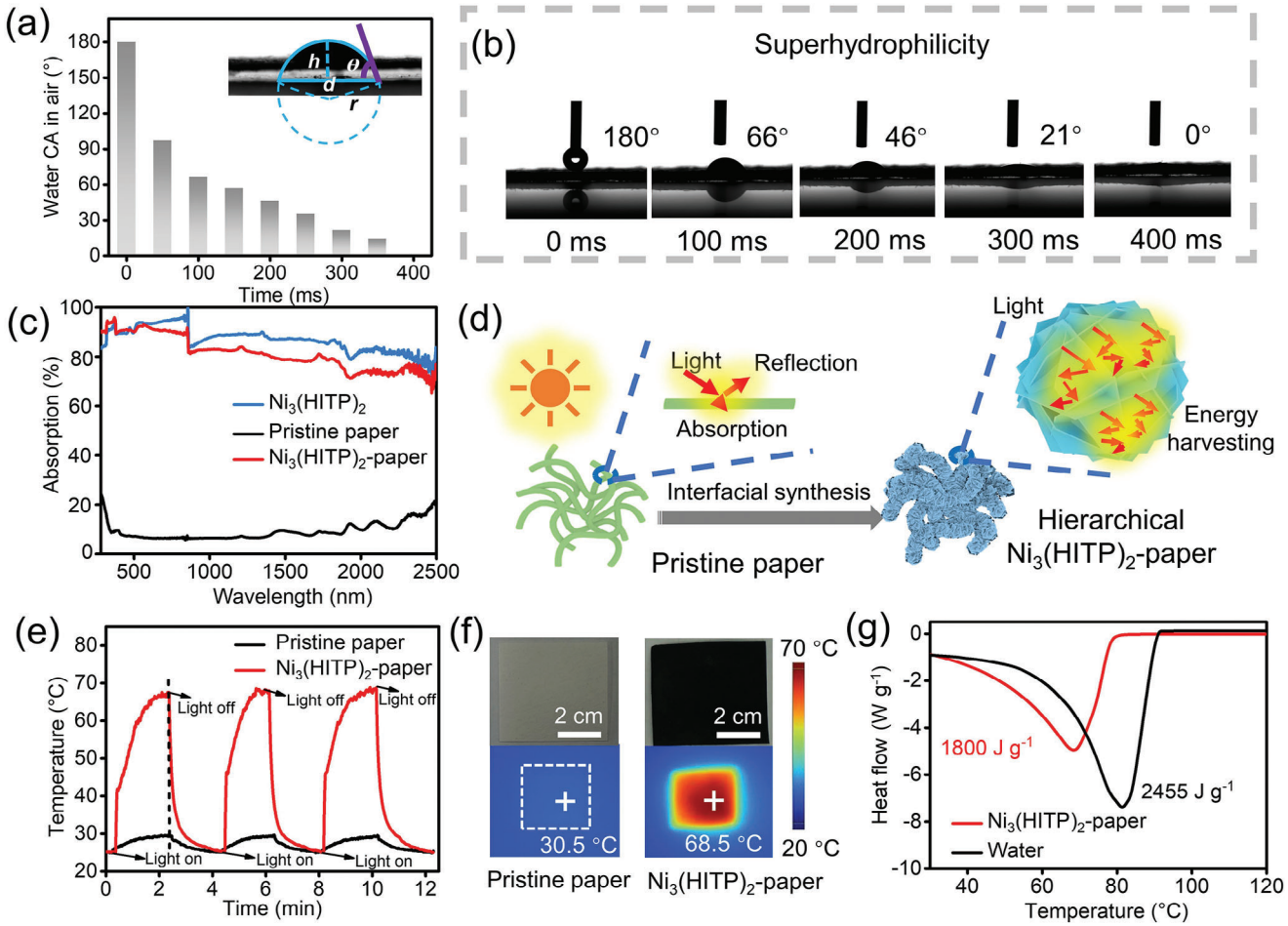

Figure 3. a) Water contact angle of $Ni_3(HITP)_2$-paper in air at different times. b) Optical photographs of the water contact angle for $Ni_3(HITP)_2$-paper at different times. c) UV–vis–NIR absorption spectra of the pristine paper, $Ni_3(HITP)_2$-paper, and $Ni_3(HITP)_2$. d) Schematic diagram of the fabrication and the solar energy harvesting of the hierarchical $Ni_3(HITP)_2$-paper nanosheets. e) Surface temperature of pristine paper and $Ni_3(HITP)_2$- paper as a function of time in dry state under 1 sun. f) Optical photographs and infrared images of the pristine paper and $Ni_3(HITP)_2$-paper in the dry state under 1 sun. g) DSC curves of pure water and $Ni_3(HITP)_2$-paper-water systems.

adsorption–desorption isotherm further confirms the microporous feature of $Ni_3(HITP)_2$. According to the pore size distribution curve, the $Ni_3(HITP)_2$ shows a narrow pore size distribution centered at ≈1.5 nm, which is consistent with the value from its crystal structure (Figure S5, Supporting Information).

To further investigate the electronic structure and chemical composition of the $Ni_3(HITP)_2$, X-ray photoelectron spectroscopy (XPS) is performed, and the result is similar to previous reports.[34,35] As shown in Figure 2e, the peaks corresponding to Ni $2p_{3/2}$, Ni $2p_{3/2}$ satellites, Ni $2p_{1/2}$, and Ni $2p_{1/2}$ satellites appear at the binding energies of 855.6, 861.4, 873.1, and 879.1 eV, respectively, indicating that Ni in $Ni_3(HITP)_2$ is Ni^{2+}. In addition, the fitted N 1s spectrum is mainly divided into three peaks with binding energies of 398.3, 399.6, and 401.0 eV, corresponding to Ni–N, graphitic-N, and N–H, respectively (Figure 2f). The fitted C 1s spectrum is divided into three peaks centered at 284.3, 285.4, and 288.1 eV. There peaks are attributed to the C—C/C=C, C—N, and C=N bonds of $Ni_3(HITP)_2$, respectively (Figure S6, Supporting Information).

To asssess the mechanical properties of $Ni_3(HITP)_2$-paper, tensile stress–strain tests are conducted, as shown in Figure S7a, Supporting Information. Pristine paper exhibits a tensile strength of 15.2 MPa and a breaking strain of 5.4%. In contrast, $Ni_3(HITP)_2$-paper displays a tensile strength of 15.4 MPa and a breaking strain of 10.9%. The Young's modulus of the paper without and with $Ni_3(HITP)_2$ decreases from 671.3 to 416.2 MPa; while, the toughness is enhanced from 0.60 to 1.28 MJ m^{-3} (Figure S7b, Supporting Information). These results demonstrate that the toughness of the paper can be enhanced by inducing growth of $Ni_3(HITP)_2$ on paper, with virtually no change in the breaking strength. This characteristic is advantageous for practical use and storage.

The water contact angle of $Ni_3(HITP)_2$-paper in air is measured as shown in **Figure 3a** (Additional details on the calculation of the water contact angle can be found in the inset and in Note S1, Supporting Information). Optical photographs illustrating the water contact angle of $Ni_3(HITP)_2$-paper at different time intervals are presented in Figure 3b. The water droplet readily spreads across the surface of $Ni_3(HITP)_2$-paper within 400 ms

under ambient conditions, ultimately achieving a water contact angle close to 0°. Hence, the $Ni_3(HITP)_2$-paper exhibits superhydrophilicity, which is a highly significant characteristic for water evaporation.

Optical absorption is a crucial parameter for evaluating the performance of photothermal materials. Therefore, enhancing the photoabsorption of photothermal conversion materials through structural design is significant. As shown in Figure 3c, pristine paper exhibits almost no photoabsorption properties. In contrast, the $Ni_3(HITP)_2$-paper shows strong absorption in the range of 280–2500 nm with a minimum absorption of ≈70% at 2470 nm and a maximum absorption of ≈90% at 377 nm. The narrower energy gap of $Ni_3(HITP)_2$ facilitates the broad-spectrum optical absorption.[36] A noteworthy aspect is that the hierarchical structure of $Ni_3(HITP)_2$-paper that efficiently increases the surface area captures sunlight and harnesses light energy through multiple reflections (Figure 3d).[10]

To explore photothermal properties, we conducted cyclic temperature response experiments on pristine paper and $Ni_3(HITP)_2$-paper under one sun (1 kW m^{-2}). As shown in Figure 3e,f, the surface temperature of $Ni_3(HITP)_2$-paper increased rapidly under light exposure and stabilized at 68.5 °C after 2 min. Upon turning off the light, the temperature quickly decreased. In contrast, the surface temperature of pristine paper could only reach to 30.5 °C. The $Ni_3(HITP)_2$-paper could repeatedly reach to 68.5 °C in three exemplary cycles. Compared with pristine paper, the $Ni_3(HITP)_2$-paper showed seven times higher photothermal conversion efficiencies with the value of 96.25% (Details of the calculations are provided in Note S2, Supporting Information).

Previous studies have shown that the porous network structures can facilitate the reduction of water evaporation enthalpy and enhance the evaporation rate.[37] In order to investigate the water evaporation enthalpy of $Ni_3(HITP)_2$-paper, thermodynamic analyses were performed on pure water and water on $Ni_3(HITP)_2$-paper. As illustrated in Figure 3g, differential scanning calorimetry (DSC) results revealed that the evaporation enthalpy of pure water was 2455 J g^{-1}, consistent with the previous report.[38] Meanwhile, the evaporation enthalpy of the water in the $Ni_3(HITP)_2$-paper-system was reduced to 1800 J g^{-1}. In bulk water, water molecules are bound by strong hydrogen bonds; and thus, require more energy to transit into gaseous water molecules.[38] Differently, $Ni_3(HITP)_2$ possesses the unique hydrophobic–hydrophilic microporous structure, which weakens the hydrogen bonding among water molecules as they pass through the nanochannel; and thus, decrease the enthalpy. In addition, considering the evaporation process of water in the actual environment, the enthalpy of evaporation of $Ni_3(HITP)_2$ paper-water and pure water in the dark environment is more reasonable, and the detailed calculation is similar to the method previously reported (Figure S8 and Note S3, Supporting Information).[12] The evaporation enthalpy estimated by the evaporation process in a dark environment (1676 J g^{-1}) showed the similar trend but lower than that obtained through the DSC method (1800 J g^{-1}). The reason for the difference is that DSC measures the process of completely dehydration, whereas actual solar water evaporation involves partial dehydration. Notably, here the evaporation enthalpy obtained by the evaporation process in a dark environment was employed in the calculation of the enthalpy change (Note S4, Supporting Information).

Similar to the biological channels of some desert plants and animals,[39] the $Ni_3(HITP)_2$ has a unique structure of alternative hydrophilic and hydrophobic channels. In particular, the amino hydrophilic sites can capture water molecules; while, the benzene ring hydrophobic channels can reduce the transport barrier of water molecules, facilitating water molecules transportation. In this study, the introduction of $Ni_3(HITP)_2$ enables $Ni_3(HITP)_2$-paper composite film to be an ideal material for water evaporation. A evaporator based on $Ni_3(HITP)_2$-paper is designed to investigate the evaporation performance under different light intensities (**Figure 4a**). The $Ni_3(HITP)_2$-paper is cut into rectangular strips and then bent to form two pins. These two pins are immersed in water through expanded polystyrene foam with slits. The optical photograph of the device is presented in Figure S9, Supporting Information. Owing to the superhydrophilic characteristic of $Ni_3(HITP)_2$-paper, water is rapidly transported to the surface of $Ni_3(HITP)_2$-paper through the two pins. When simulated sunlight vertically irradiates onto the evaporator, the solar energy is directly converted into heat energy, enabling the liquid water transition into vapor. Mass changes are continuously monitored in real-time during the evaporation process using an electronic balance, and detailed testing procedures are provided in the Experimental Section. Meanwhile, the surface temperature versus time curves for $Ni_3(HITP)_2$-paper are measured and plotted under different light intensities. As shown in Figure 4b–e, within the initial 10 min, the surface temperature of $Ni_3(HITP)_2$-paper rapidly increases from 20 °C to 40.3 °C (1 kW m^{-2}), 54.5 °C (3 kW m^{-2}), 60.6 °C (5 kW m^{-2}), 69.8 °C (7 kW m^{-2}), and 81.0 °C (10 kW m^{-2}), respectively; and then, remains stable. Clearly, the evaporation rate of $Ni_3(HITP)_2$-paper greatly surpasses that of pure water under different light intensities (1 kW m^{-2}, 0.59 kg m^{-2} h^{-1}), as depicted in Figure 4c. Specifically, the evaporation rate of $Ni_3(HITP)_2$-paper is 1.61, 4.7, 7.81, 10.8, and 15.1 kg m^{-2} h^{-1} under diverse light intensities (1–10 kW m^{-2}), respectively. Remarkably, the evaporation rate of $Ni_3(HITP)_2$-paper surpasses the thermodynamic limit (1.47 kg m^{-2} h^{-1}) at a light intensity of 1 kW m^{-2}, possibly due to the lower water evaporation enthalpy. Specifically, the hydrophilic sites of $Ni_3(HITP)_2$ form hydrogen bonds with water molecules, weakening the interactions within the water molecules and allowing them to transform from liquid to gaseous state in lower energy. In contrast, hydrophobic channels reduce the affinity between water molecules and channels, reducing the transport barrier for water molecules. Figure S10, Supporting Information provides the mass change rates versus time curves for $Ni_3(HITP)_2$-paper under different light intensities. The results indicate that the mass change rates significantly increase with increasing light intensity and stabilized within 10 min. Further, the amount of vapor on the surface of $Ni_3(HITP)_2$-paper quickly increases and is visible to naked eyes (Figure 4d). The corresponding infrared images are shown in Figure 4e. The conversion efficiencies of $Ni_3(HITP)_2$-paper are 71.1%, 75.0%, 76.4%, 76.8%, and 76.7% under different light intensities (Figure 4f). It is important to note that these calculations deduct the mass change associated with dark evaporation (Note S5, Supporting Information).

The heat loss of $Ni_3(HITP)_2$-paper under different light intensities is further calculated. Generally, the heat loss involves

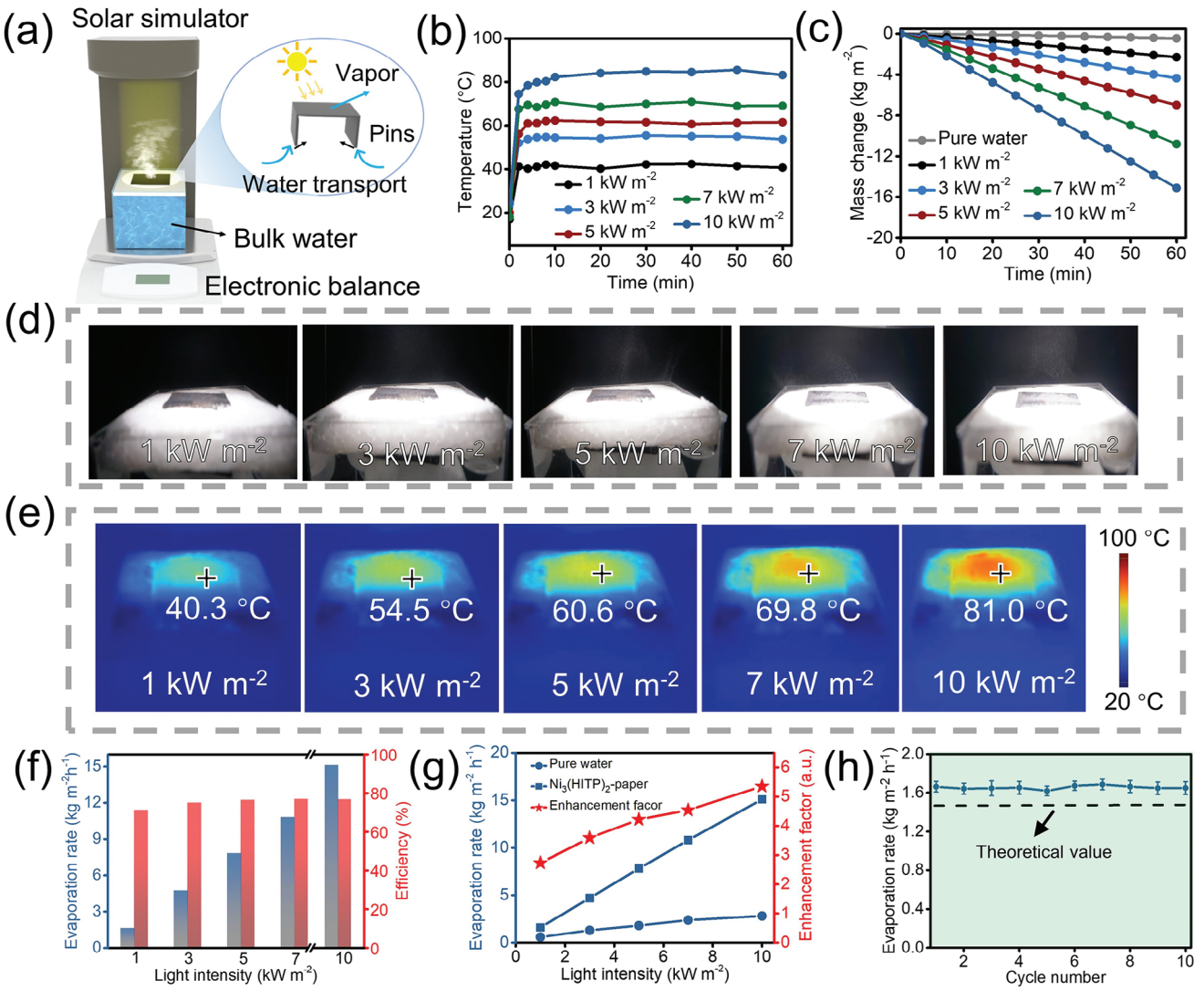

Figure 4. a) Schematic diagram of a solar water evaporation system for a $Ni_3(HITP)_2$-paper-based evaporator. b) Surface temperature of $Ni_3(HITP)_2$-paper as a function of time under different light intensities. c) Mass change of pure water as a function of time under light intensity of 1 kW m^{-2} and mass change of $Ni_3(HITP)_2$-paper as a function of time under different light intensities. d) Optical photographs of the vapor on the surface of $Ni_3(HITP)_2$-paper under different light intensities. e) Infrared images of $Ni_3(HITP)_2$-paper under different light intensities. f) Evaporation rate and conversion efficiency of $Ni_3(HITP)_2$-paper under different light intensities. g) Enhancement factor of the evaporation rate of $Ni_3(HITP)_2$-paper compared to pure water and the corresponding evaporation rate under different light intensities. h) Stability test of the evaporation rate of $Ni_3(HITP)_2$-paper under 1 kW m^{-2} over ten cycles.

radiation loss, convection loss, and conduction loss. Here, taking the heat loss from a light intensity of 1 kW m^{-2} as an example, the total heat loss is 28.9%; among these losses, the radiation loss is 8.1%, the convection loss is 7.4%, and the conduction loss is 13.4% (Detailed calculations are provided in Note S6, Supporting Information). This heat loss is remarkably lower than that of typical exfoliated graphite (36%) and graphene oxide materials (50%) and is similar to that of MXene (29%).[2,14,40] The lesser heat loss is attributed to the low thermal conductivity of $Ni_3(HITP)_2$.[41] Therefore, the use of low thermal conductivity material is an effective strategy to optimize evaporation efficiency in the future.

To further visualize the advantages of $Ni_3(HITP)_2$-paper in solar water evaporation, the enhancement factor of evaporation rate for $Ni_3(HITP)_2$-paper compared to pure water (Figure S11, Supporting Information) under different light intensities is calculated, as shown in Figure 4g. The enhancement factors are 2.73, 3.59, 4.31, 4.53, and 5.35 under light intensities of 1, 3, 5, 7, and 10 kW m^{-2}, respectively. Meanwhile, cyclic stability is an important property of a device. Therefore, long-term water evaporation cycle experiments of $Ni_3(HITP)_2$-paper-based evaporator are performed. As shown in Figure 4h, the evaporation rates remain 1.6 kg m^{-2} h^{-1} over ten cycles without significant decrease.

It is worth noting that many reported solar evaporators tend to experience a gradual decrease in evaporation rate during desalination, which is attributed to salt crystallization blocking the surface of the photothermal material and the water transport channels.[42,43] Therefore, enhancing the durability of evaporation systems in saline environments for solar-driven desalination

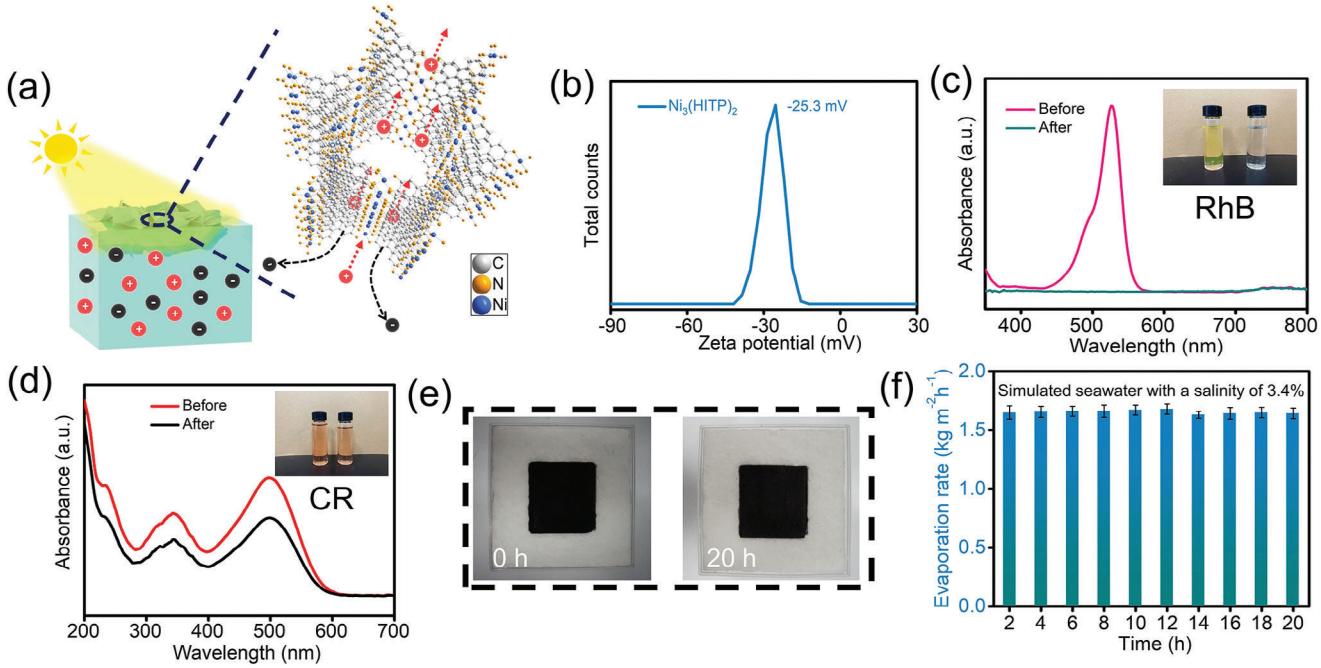

Figure 5. Salt resistance properties of $Ni_3(HITP)_2$. a) Schematic of the salt resistance mechanism for hierarchical $Ni_3(HITP)_2$ nanosheets with 1D charged channels. b) Zeta potential of $Ni_3(HITP)_2$. c) Absorption spectra of RhB before and after $Ni_3(HITP)_2$ powders treatment. d) Absorption spectra of CR before and after $Ni_3(HITP)_2$ powders treatment. e) Optical photographs of $Ni_3(HITP)_2$-paper-based evaporator before and after 20 h of evaporation in simulated seawater. f) Evaporation rate of $Ni_3(HITP)_2$-paper-based evaporator for a duration of 20 h under 1 kW m^{-2}.

is an attractive prospect. Charged channels allow one ion to pass through and repel another, effectively preventing the salt from crystallizing on the surface of the material (**Figure 5**a). Figure 5b demonstrates that the zeta potential of $Ni_3(HITP)_2$ in simulated seawater is −25.3 mV, indicating the channel in $Ni_3(HITP)_2$ is negatively charged. To bolster the reliability of these findings, we verify the charged nature of the channel surfaces of $Ni_3(HITP)_2$ from the perspective of electrostatic interactions using polar dyes. Figure 5c shows the ultraviolet–visible absorption spectra of the cationic dye rhodamine B (RhB) before and after treatment with $Ni_3(HITP)_2$ powders. The initial RhB solution exhibits high absorbance at 527 nm; while, the absorbance of the solution after immersion in $Ni_3(HITP)_2$ powders is close to zero. In contrast, Congo red (CR) cannot be adsorbed by $Ni_3(HITP)_2$ powders due to mutual repulsion resulting from their negative electrical properties (Figure 5d). The difference in absorbance of the CR aqueous solution before and after treatment may be attributed to the physical adsorption of $Ni_3(HITP)_2$. The results validate the charged nature and ion-selective advantages of $Ni_3(HITP)_2$ nanochannels.

To confirm the salt resistance of $Ni_3(HITP)_2$-paper-based evaporators, we further assessed the durability of the system using simulated seawater (salinity 3.4%), as demonstrated in Figure 5e,f. There was no salt accumulation on the surface of $Ni_3(HITP)_2$-paper even after 20 h of operation. Simultaneously, the evaporation rate of $Ni_3(HITP)_2$-paper did not significantly decrease for a duration of 20 h under 1 kW m^{-2}. Besides the desalination from regular concentration (3.4%) of simulated seawater, the sustainable salinity resistance of highly concentrated (20%) simulated seawater was also essential.[44] The results show that even upon continuous desalination in such high concentration of simulated seawater for over 20 h, the evaporation rate of ≈1.6 kg m^{-2} h^{-1} was successfully retained (under 1 sun), while no salt was observed on the surface of $Ni_3(HITP)_2$-paper (Figure S12, Supporting Information).

In order to evaluate the practicality of $Ni_3(HITP)_2$-paper evaporator, a prototype has been elaborately built. The outdoor tests were performed at the Qishan Campus (26.0261 °N, 119.2104 °E), Fujian Normal University, Fuzhou, China, on Nov. 17th, 2023. As shown in **Figure 6**a, water vapor was rapidly generated upon natural sunlight irradiation for 10 min, and a layer of condensed water immediately formed on the inner wall of the glass dome. Moreover, the desalination performance of the $Ni_3(HITP)_2$-paper evaporator under natural sunlight was investigated by simulated seawater (salinity of 3.4%). The salinity of the clean water collected from the $Ni_3(HITP)_2$-paper evaporation system was measured by inductively coupled plasma optical emission spectrometer (ICP-OES), as shown in Figure 6b. Compared to the initial simulated seawater, the concentrations of Na^+, Mg^{2+}, Ca^{2+}, and K^+ in the desalinated clean water were reduced by 2–4 orders of magnitude, which meets the ionic standards for drinking water determined by the World Health Organization (WHO). We recorded the weather conditions of the outdoor evaporation test device, including light intensity, ambient temperature, and ambient relative humidity (Figure 6c,d) under outdoor testing monitored by time on a sunny day from 9:00–16:00. The evaporation rate of the $Ni_3(HITP)_2$-paper evaporator was positively correlated with the sunlight intensity (Figure 6d) and the evaporator was working perfectly well under actual conditions.

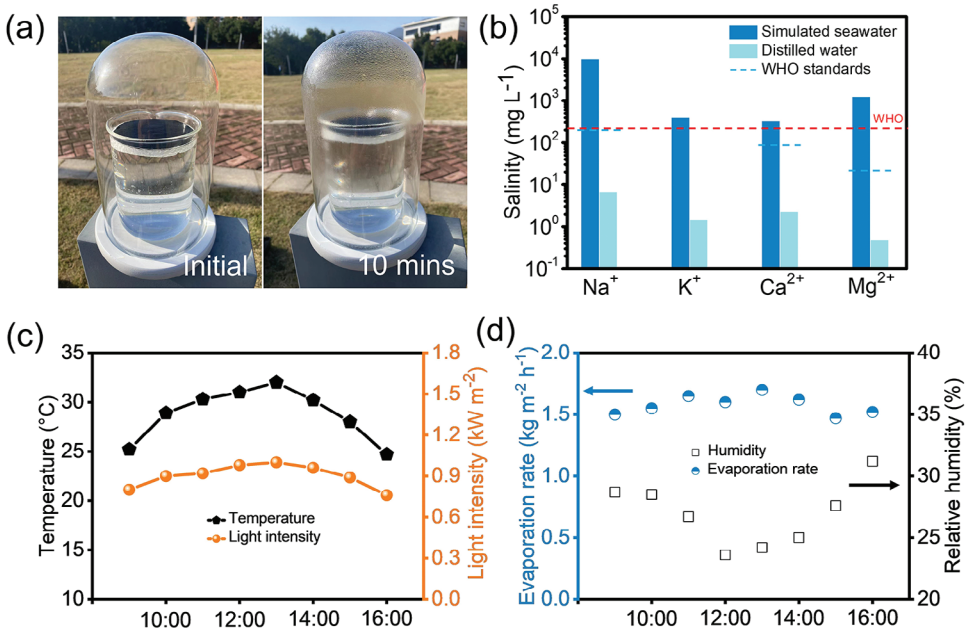

Figure 6. a) Optical photographs showing the collection device for solar evaporation and the condensation of clean water on the inner wall of the glass dome. b) Ion concentrations of the original simulated seawater and the distilled water collected during solar evaporation. c) Light intensity and ambient temperature during outdoor testing. d) Ambient relative humidity and evaporation rate of $Ni_3(HITP)_2$-paper evaporator under outdoor testing monitored by time on a sunny day from 9:00–16:00.

Different from the strategy of enhancing the evaporation performance of evaporators through system and macrostructure design,[45–47] the electric-assisted solar evaporation is favorable to address the demand issues in real scenarios. First, electric-assisted solar evaporation can alleviate the time-dependence of the evaporator on sunlight and achieve all-weather operation, which solves the problem of poor evaporation performance of the evaporator in environments of insufficient light, such as cloudy or rainy day and at night. Second, electric-assisted evaporation can well overcome the problem of the existence of thermodynamic limit of evaporation in solar evaporators and significantly improve the evaporation performance. Third, power equipment based on novel clean energy sources (e.g., solar, wind, and hydroelectric) can be used for electric-assisted solar evaporation in the future, which is more attractive to alleviate the problem of global freshwater shortage. Therefore, an all-weather, efficient water evaporation system based on $Ni_3(HITP)_2$-paper is designed to integrate solar energy with other power supply devices, as illustrated in **Figure** 7a. This system can be used to evaporate water at night using the Joule-heating effect; while, harnessing the synergistic effects of photothermal and Joule-heating for water evaporation during the day. To evaluate the Joule-heating performance of the evaporator, the surface temperature of the wetted $Ni_3(HITP)_2$-paper was monitored under different input electrical powers, as shown in Figure 7b. The results demonstrated that when a voltage was applied at both ends of $Ni_3(HITP)_2$-paper, electrons flowed through the $Ni_3(HITP)_2$-paper, generating Joule-heating to raise the temperature of the $Ni_3(HITP)_2$-paper.

The surface temperature of $Ni_3(HITP)_2$-paper stabilized within 10 min. Specifically, the surface temperature of $Ni_3(HITP)_2$-paper increased from 22.4 °C to 26.2 °C, 30.6 °C, 35.5 °C, and 38.1 °C, when the input electrical power was 0, 0.3, 1.0, 2.3, and 4.0 W, respectively, as depicted in Figure 7c. The mass change of the system increased from 0.14 to 0.20, 0.32, 0.51, and 0.71 kg m^{-2} (Figure 7d), respectively. These results indicated that the water evaporation performance of $Ni_3(HITP)_2$-paper could occur by the Joule-heating effect, even in the absence of solar irradiation. The calculations of electrical power-steam conversion efficiency are provided in Note S7, Supporting Information. The stable surface temperature of $Ni_3(HITP)_2$-paper also clearly rose with the increase of the input electrical power at both ends under the synergistic effects of photothermal and Joule-heating (Figure 7e). Specifically, the surface temperature of $Ni_3(HITP)_2$-paper increased from 40.3 °C to 42.1 °C, 44.4 °C, 46.5 °C, and 48.7 °C under one sun plus input electrical powers of 0.3, 1.0, 2.3, and 4.0 W, respectively (Figure S13, Supporting Information). The mass change of the system increased from 1.61 to 2.60 kg m^{-2} under 1 kW m^{-2} when the input electrical power was elevated from 0 to 4.0 W (Figure 7f). Figure 7g illustrates the evaporation rate (ER) and enhancement percentage of evaporation rate for $Ni_3(HITP)_2$-paper under one sun plus different input electrical powers, respectively. Obviously, the evaporation rate was increased by over 60% under one sun when the input electrical power was raised from 0 to 4.0 W.

Remarkably, the evaporation rate achieved by $Ni_3(HITP)_2$-paper, driven by the combination of light intensity of 1 kW m^{-2} plus input electrical power of 4.0 W, surpasses previously reported for 2D structure MOF-based evaporators (Table S1, Supporting Information). In addition, considering the advantages of construction and process design in enhancing evaporation performance, the 3D structure $Ni_3(HITP)_2$-paper evaporator is expected to obtain higher performance in the future.[48–52] Interestingly, the evaporation rate (2.60 kg m^{-2} h^{-1}) outperforms the sum of the evaporation rates obtained through only electric

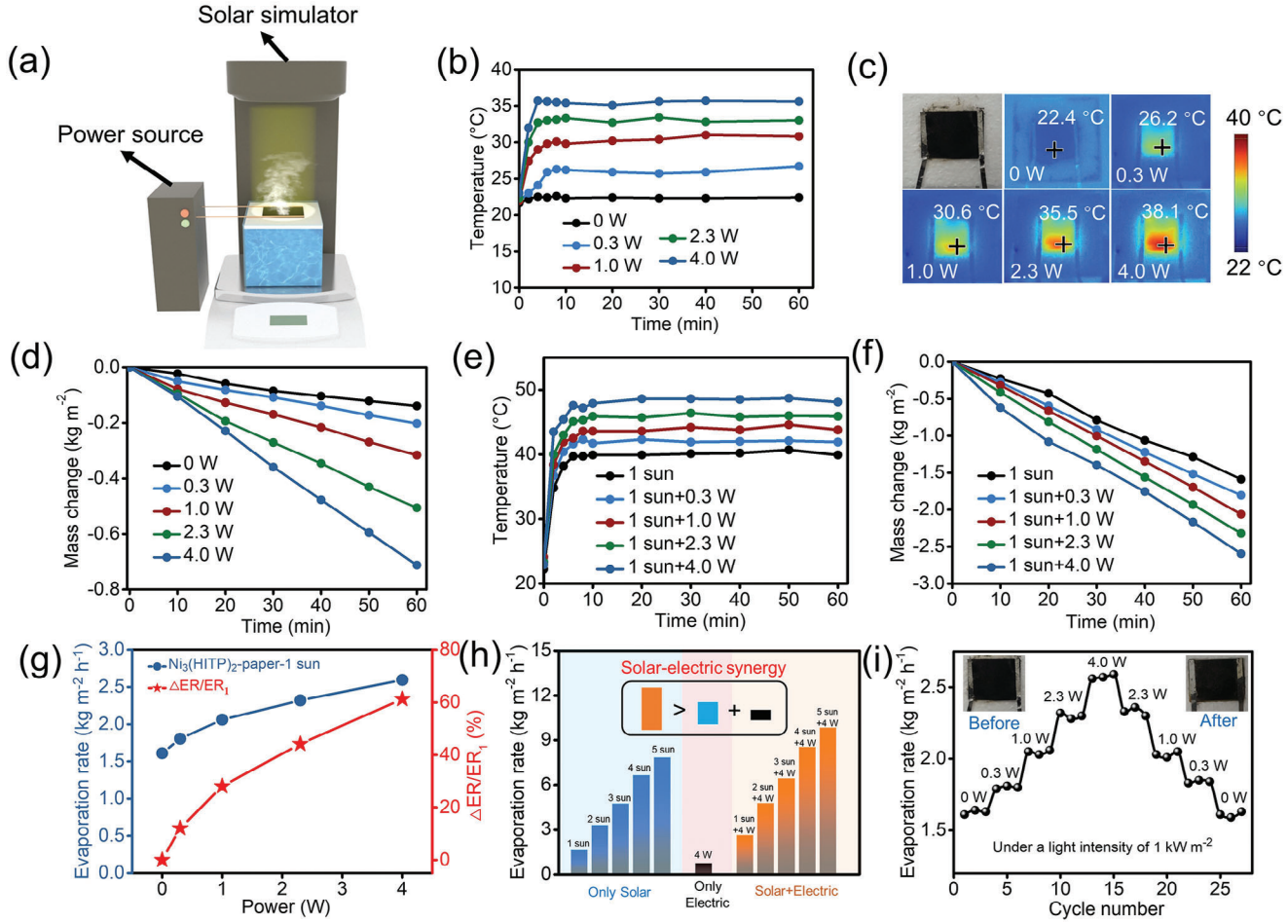

Figure 7. a) Schematic diagram of a $Ni_3(HITP)_2$-paper-based solar evaporation system with synergistic photothermal and Joule-heating effects. b) Surface temperature as a function of time for $Ni_3(HITP)_2$-paper under different input electrical powers. c) Optical photograph and infrared images of $Ni_3(HITP)_2$-paper under different input electrical powers. d) Mass change of $Ni_3(HITP)_2$-paper as a function of time under different input electrical powers. e) Surface temperature of $Ni_3(HITP)_2$-paper under one sun plus different input electrical powers (0–4.0 W), respectively. f) Mass change curves of $Ni_3(HITP)_2$-paper as a function of time under one sun plus different input electrical powers (0–4.0 W), respectively. g) Evaporation rate and the corresponding enhancement percentage of the evaporation rate of $Ni_3(HITP)_2$-paper under one sun plus different input electrical powers (0–4.0 W), respectively. △ER represents the change of evaporation rate under one sun plus the input electrical powers, respectively, compared to that of the initial condition under only one sun. ER_1 corresponds to the evaporation rate under only one sun. h) Evaporation rate of $Ni_3(HITP)_2$-paper under only solar energy; only input electrical power of 4 W and solar-electric energy synergy. i) Evaporation rate of $Ni_3(HITP)_2$-paper under one sun plus different input electrical powers (0–4.0 W), respectively. Inset: optical photographs of $Ni_3(HITP)_2$-paper before and after cycling.

energy-driven (0.71 kg m^{-2} h^{-1}) and only solar energy-driven (1.61 kg m^{-2} h^{-1}). This phenomenon is attributed to the solar-electric energy synergistic enhancement effects. Specifically, additional Joule-heating elevates the surface temperature of the evaporator; while, solar irradiation reduces the ambient relative humidity above the sample.[6] These two factors promote the liquid water-steam conversion and the escape of steam. In addition, the same trend can be found with increased light intensity to 2 kW m^{-2} (from 3.28 to 4.74 kg m^{-2}) (Figure S14, Supporting Information). More importantly, we found that this synergistic enhancement effect is more significant with increasing light intensity under the same input electrical power (4 W). In particular, the evaporation rate increased from 4.7 to 6.4 kg m^{-2} h^{-1}, 6.62 to 8.5 kg m^{-2} h^{-1}, and 7.81 to 9.8 kg m^{-2} h^{-1} when the light intensity was 3, 4, and 5 kW m^{-2}, respectively (Figure 7h). Further, the modulation of input electrical power demonstrated highly stable and controllable changes in the evaporation rate of $Ni_3(HITP)_2$-paper (Figure 7i). It is worth noting that $Ni_3(HITP)_2$-paper exhibited no significant damage after multiple testing cycles, as shown in the inset, indicating its reusability.

3. Conclusion

In summary, the large-area high-quality hierarchical macro/microporous $Ni_3(HITP)_2$ nanosheet film was successfully designed and prepared on flexible paper substrate. Due to its broad-spectrum absorption, low thermal conductivity, and excellent conductivity, we have applied it to an all-weather efficient water evaporator. The hydrophobic nano-channels and hydrophilic sites in $Ni_3(HITP)_2$ significantly reduced water evaporation enthalpy to 1676 J g^{-1} (significantly lower than the evaporation enthalpy of pure water 2455 J g^{-1}). Hierarchical

$Ni_3(HITP)_2$ nanosheets with certain orientation on the surface of paper fibers increased the surface area of the composite film and enhanced the effective solar energy capture by multiple reflections, resulting in remarkable photothermal conversion efficiencies of up to 96.25%. Combining with the excellent electrical properties of $Ni_3(HITP)_2$, $Ni_3(HITP)_2$-paper films were utilized to synergize with the photothermal and Joule-heating effects, resulting in a further enhancement of the water evaporation rate to 2.60 kg m^{-2} h^{-1}, exceeding that of other MOF-based materials. This photovoltaic-coupled evaporator could operate round the clock, effectively mitigating climate-related issues. The negative charged nanochannels in $Ni_3(HITP)_2$ nanosheets enabled the $Ni_3(HITP)_2$-paper films selective separation of salt ions and water to prevent salt crystallization. This research provides valuable insights into the development of all-weather, portable, and scalable devices for efficient water evaporation.

4. Experimental Section

Materials: All chemicals were purchased through commercial suppliers and used without further purification. Nickel chloride hexahydrate, absolute ethanol, and ammonium hydroxide were purchased from Adamas. 2,3,6,7,10,11-hexaaminotriphenylene hexahydrochloride could be prepared according to the procedure in previous work. Commercial filter paper (thickness ≈ 180 µm) was purchased online. Deionized water was used for all water.

Preparation of Simulated Seawater: The simulated seawater with a salinity of 3.4% was prepared by adding NaCl (27.23 g), $MgCl_2$ (10.78 g), $CaCO_3$ (1.00 g), and K_2SO_4 (0.89 g) to 1 L of deionized water and stirring for 1 h. The simulated seawater with a salinity of 20% was prepared by the similar process.

Preparation of $Ni_3(HITP)_2$-Paper Composites: Here, an interface-induced growth method was used. Specifically, the nickel (II) chloride hexahydrate and HITP (2,3,6,7,10,11-hexaaminotriphenylene) were added to deionized water in the weight ratio of 0.66:1. Under continuous stirring under air atmosphere, the paper was inserted obliquely into the mixture. Then, ammonium hydroxide (4 mL) was added to the above mixture, and the reaction was carried out at 65 °C for 2 h. Afterward, the $Ni_3(HITP)_2$-paper composite film was washed with ethanol and deionized water, respectively. Finally, the $Ni_3(HITP)_2$-paper composite was dried under vacuum at 30 °C.

Measurement of Solar Water Evaporation: Here, the solar water evaporation device was a container measuring 6 cm × 6 cm × 5.5 cm (length × width × height). First, a $Ni_3(HITP)_2$-paper (thickness of 190 µm) with dimensions of 2.5 cm × 5.5 cm was fixed in the middle of an expanded polystyrene foam (thickness of 0.5 cm) with dimensions of 6 cm × 6 cm. The extra part was used as pins at the ends of the evaporator, which had dimensions of 2.5 cm × 1.5 cm, that is, an effective area of 3.75 cm^2. It was noted that a foam of 2.5 cm × 2.5 cm was placed on the bottom of the $Ni_3(HITP)_2$-paper in order to limit the heat transfer losses between the evaporator and the bulk water. The intensity of the simulated light source was calibrated by a light power meter. The solar water evaporation device was exposed to different intensities of simulated sunlight for 60 min, where the mass changes were recorded in real-time by an electronic balance. The temperature changes of the $Ni_3(HITP)_2$-paper surface were recorded with an infrared thermometer. The evaporation experimental tests were conducted indoors in an open environment at a temperature of 25 °C and relative humidity of ≈40%.

Melting Behavior of $Ni_3(HITP)_2$-Paper by DSC Measurement: During the experiments, $Ni_3(HITP)_2$-paper and pure water were placed separately in a sealed aluminium crucible to prevent evaporation of the water. Further, the measurement was performed at a linear heating rate of 5 °C min^{-1} under a nitrogen flow rate (50 mL min^{-1}) in the temperature range of 20 °C to 120 °C.

Measurement of the Zeta Potential of $Ni_3(HITP)_2$: $Ni_3(HITP)_2$ powders were homogeneously dispersed in simulated seawater (pH ≈ 8, salinity of 3.4%) in a Malvern potentiostat cuvette, and the Zeta potential values were recorded by a ZETA potential analyzer at room temperature of 25 °C.

Characterizations: SEM images were observed by a field emission scanning electron microscope (Hitachi SU-8010). UV–vis–NIR absorption spectra were recorded by a UV–vis–NIR spectrophotometer (Lambda 950). X-ray diffraction (XRD) patterns were measured with a Rigaku Ultima IV, Japan, with Cu *Kα* radiation ($\lambda = 0.15\ 405$ nm) operating at 40 kV and 40 mA. The evaporation enthalpy was measured by differential scanning calorimetry (DSC ta250). Zeta potential was characterized by a ZETA potential analyzer (Malvern NANO ZSE). The contact angle between the absorber and water was calculated by means of a dynamic contact angle tester (KRUSS DSA25, Germany). Mechanical properties were analyzed using the material testing machine (INSTRON 3343). The infrared images were recorded by an infrared camera (Fluke Ti10). The optical photographs were recorded with a digital camera (SONY ILCE 6000). Mass changes during evaporation were recorded by an electronic balance (AH-A+R303H). The light intensity was calibrated by an optical radiometer (PerfectLight-MW 2000). Simulated sunlight was provided by a solar simulator (PLS-SXE 300). Temperature data were recorded by using a laser-sighted infrared thermometer (Optris LS). Metal ion concentration was measured by inductively coupled plasma optical emission spectrometer (ICP-OES, Avio 200 Max). The nitrogen sorption isotherms were measured at liquid nitrogen temperature of 77 K using an automatic volumetric adsorption equipment (Belsorp Max) after degassing it at 100 °C for 12 h. The pore size distribution was simulated using the nonlocal density functional theory model.

Supporting Information

Supporting Information is available from the Wiley Online Library or from the author.

Acknowledgements

The authors acknowledge the National Natural Science Foundation of China (22325109, 52373113, 22271281, 21975254, 22171263, 91961115), the Natural Science Foundation of Fujian Province (2021J02017, 2020J02036 and 2022J06032), the Scientific Instrument Developing Project of the Chinese Academy of Sciences (YJKYQ20210024), the Top Young Talents Program of Fujian Province and Future-prospective and Stride-across Programs of HaixiInstitutes, Chinese Academy of Sciences (CXZX-2022-JQ03).

Conflict of Interest

The authors declare no conflict of interest.

Author Contributions

Y.Q. and L.C. planned and designed the project. Y.Q. and G.F.X. conducted all the experiments, analyzed the data, and wrote the paper. G.-E.W. helped to synthesize the materials and characterize the samples. L.C., G.X., and G.-E.W. directed the writing of the paper. L.C., G.-E.W., and G.X. supervised the project.

Data Availability Statement

The data that support the findings of this study are available from the corresponding author upon reasonable request.

Keywords

conductive metal–organic framework, hierarchical structure nanosheet, thin film, water evaporation

Received: October 16, 2023
Revised: December 3, 2023
Published online:

[1] M. A. Shannon, P. W. Bohn, M. Elimelech, J. G. Georgiadis, B. J. Mariñas, A. M. Mayes, *Nature* **2008**, *452*, 301.
[2] H. Ghasemi, G. Ni, A. M. Marconnet, J. Loomis, S. Yerci, N. Miljkovic, G. Chen, *Nat. Commun.* **2014**, *5*, 4449.
[3] P. Liu, Y. B. Hu, X. Y. Li, L. Xu, C. Chen, B. Yuan, M. L. Fu, *Angew. Chem., Int. Ed.* **2022**, *61*, 202208587.
[4] X. Li, J. Li, J. Lu, N. Xu, C. Chen, X. Min, B. Zhu, H. Li, L. Zhou, S. Zhu, T. Zhang, J. Zhu, *Joule* **2018**, *2*, 1331.
[5] F. Liu, B. Zhao, W. Wu, H. Yang, Y. Ning, Y. Lai, R. Bradley, *Adv. Funct. Mater.* **2018**, *28*, 1803266.
[6] X. Zhao, L.i-M. Peng, C.-Y. Tang, J.-H. Pu, X.-J. Zha, K. Ke, R.-Y. Bao, M.-B. Yang, W. Yang, *Mater. Horiz.* **2020**, *7*, 855.
[7] L. Cui, P. Zhang, Y. Xiao, Y. Liang, H. Liang, Z. Cheng, L. Qu, *Adv. Mater.* **2018**, *30*, 1706805.
[8] H. Song, Y. Liu, Z. Liu, M. H. Singer, C. Li, A. R. Cheney, D. Ji, L. Zhou, N. Zhang, X. Zeng, Z. Bei, Z. Yu, S. Jiang, Q. Gan, *Adv. Sci.* **2018**, *5*, 1800222.
[9] Z. Xie, Y. Duo, Z. Lin, T. Fan, C. Xing, L. Yu, R. Wang, M. Qiu, Y. Zhang, Y. Zhao, X. Yan, H. Zhang, *Adv. Sci.* **2020**, *7*, 1902236.
[10] Z. Liu, Z. Zhou, N. Wu, R. Zhang, B. Zhu, H. Jin, Y. Zhang, M. Zhu, Z. Chen, *ACS Nano* **2021**, *15*, 13007.
[11] M.-Q. Yang, C. F. Tan, W. Lu, K. Zeng, G. W. Ho, *Adv. Funct. Mater.* **2020**, *30*, 2004460.
[12] Q. Lu, W. Shi, H. Yang, X. Wang, *Adv. Mater.* **2020**, *32*, 2001544.
[13] R. Li, L. Zhang, L. Shi, P. Wang, *ACS Nano* **2017**, *11*, 3752.
[14] J. Yang, Y. Pang, W. Huang, S. K. Shaw, J. Schiffbauer, M. A. Pillers, X. Mu, S. Luo, T. Zhang, Y. Huang, G. Li, S. Ptasinska, M. Lieberman, T. Luo, *ACS Nano* **2017**, *11*, 5510.
[15] W. He, L. Zhou, M. Wang, Y. Cao, X. Chen, X. Hou, *Sci. Bull.* **2021**, *66*, 1472.
[16] A. R. Parker, C. R. Lawrence, *Nature* **2001**, *414*, 33.
[17] J. Ju, H. Bai, Y. Zheng, T. Zhao, R. Fang, L. Jiang, *Nat. Commun.* **2012**, *3*, 1247.
[18] H. Kim, S. Yang, S. R. Rao, S. Narayanan, E. A. Kapustin, H. Furukawa, A. S. Umans, O. M. Yaghi, E. N. Wang, *Science* **2017**, *356*, 430.
[19] M. Yang, S.-Q. Wang, Z. Liu, Y. Chen, M. J. Zaworotko, P. Cheng, J.-G. Ma, Z. Zhang, *J. Am. Chem. Soc.* **2021**, *143*, 7732.
[20] Q. Ma, P. Yin, M. Zhao, Z. Luo, Y. Huang, Q. He, Y. Yu, Z. Liu, Z. Hu, B. Chen, H. Zhang, *Adv. Mater.* **2019**, *31*, 1808249.
[21] S. Cao, A. Thomas, C. Li, *Angew. Chem., Int. Ed.* **2023**, *62*, 202214391.
[22] S. Zhou, Z. Qiu, M. Strømme, C. Xu, *Energy Environ. Sci.* **2021**, *14*, 900.
[23] S. Zhou, X. Kong, M. Strømme, C. Xu, *ACS Mater. Lett.* **2022**, *4*, 1058.
[24] D. Sheberla, L. Sun, M. A. Blood-Forsythe, S. Er, C. R. Wade, C. K. Brozek, A. Aspuru-Guzik, M. Dinca, *J. Am. Chem. Soc.* **2014**, *136*, 8859.
[25] Y. Zang, F. Pei, J. Huang, Z. Fu, G. Xu, X. Fang, *Adv. Energy Mater.* **2018**, *8*, 1802052.
[26] W. Zhao, T. Chen, W. Wang, B. Jin, J. Peng, S. Bi, M. Jiang, S. Liu, Q. Zhao, W. Huang, *Sci. Bull.* **2020**, *65*, 1803.
[27] Y. Li, R. Wang, G.-E. Wang, S. Feng, W. Shi, Y. Cheng, L. Shi, K. Fu, J. Sun, *ACS Nano* **2022**, *16*, 473.
[28] E. M. Miner, T. Fukushima, D. Sheberla, L. Sun, Y. Surendranath, M. Dinca, *Nat. Commun.* **2016**, *7*, 10942.
[29] L. Sun, M. G. Campbell, M. Dinca, *Angew. Chem., Int. Ed.* **2016**, *55*, 3566.
[30] G. Wu, J. Huang, Y. Zang, J. He, G. Xu, *J. Am. Chem. Soc.* **2017**, *139*, 1360.
[31] Q. Pang, X. Liang, C. Y. Kwok, L. F. Nazar, *Nat. Energy* **2016**, *1*, 16132.
[32] C. Sun, D. Sheng, B. Wang, X. Feng, *Angew. Chem., Int. Ed.* **2023**, *62*, 202303378.
[33] D. Ghim, Q. Jiang, S. Cao, S. Singamaneni, Y.-S. Jun, *Nano Energy* **2018**, *53*, 949.
[34] D. Cai, M. Lu, L. Li, J. Cao, D. Chen, H. Tu, J. Li, W. Han, *Small* **2019**, *15*, 1902605.
[35] M. Lu, G. Wang, X. Yang, B. Hou, *Nano Res.* **2022**, *15*, 6112.
[36] M. Wang, R. Dong, X. Feng, *Chem. Soc. Rev.* **2021**, *50*, 2764.
[37] F. Zhao, Y. Guo, X. Zhou, W. Shi, G. Yu, *Nat. Rev. Mater.* **2020**, *5*, 388.
[38] X. Zhou, F. Zhao, Y. Guo, Y. Zhang, G. Yu, *Energy Environ. Sci.* **2018**, *11*, 1985.
[39] X. Ji, Y. Jiang, T. Liu, S. Lin, A. Du, *Cell Rep. Phys. Sci.* **2022**, *3*, 100815.
[40] J. Zhao, Y. Yang, C. Yang, Y. Tian, Y. Han, J. Liu, X. Yin, W. Que, *J. Mater. Chem. A* **2018**, *6*, 16196.
[41] P. Tao, G. Ni, C. Song, W. Shang, J. Wu, J. Zhu, G. Chen, T. Deng, *Nat. Energy* **2018**, *3*, 1031.
[42] C. Chen, Y. Kuang, L. Hu, *Joule* **2019**, *3*, 683.
[43] X. Zhou, F. Zhao, P. Zhang, G. Yu, *ACS Mater. Lett.* **2021**, *3*, 1112.
[44] X. Chen, Z. Wu, D. Lai, M. Zheng, L. Xu, J. Huo, Z. Chen, B. Yuan, M.-L. Fu, *J. Mater. Chem. A* **2020**, *8*, 22645.
[45] H. Wang, C. Zhang, Z. Zhang, B. Zhou, J. Shen, A. Du, *Adv. Funct. Mater.* **2020**, *30*, 2005513.
[46] Y. Gao, Q. Sun, Y. Chen, X. Zhou, C. Wei, L. Lyu, *Chem. Eng. J.* **2023**, *455*, 140500.
[47] Y. Xu, J. Xu, J. Zhang, X. Li, B. Fu, C. Song, W. Shang, P. Tao, T. Deng, *Nano Energy* **2022**, *93*, 106882.
[48] H. Wang, C. Zhang, A. Du, *Sol. RRL* **2023**, *7*, 2201128.
[49] H.-C. Yang, F. Lu, H.-N. Li, C. Zhang, S. B. Darling, Z.-K. Xu, *Adv. Funct. Mater.* **2023**, *33*, 2304580.
[50] Z.-Y. Wang, Y.-J. Zhu, Y.-Q. Chen, H.-P. Yu, Z.-C. Xiong, *Small* **2023**, *19*, 2206917.
[51] C. Li, B. Zhu, Z. Liu, J. Zhao, R. Meng, L. Zhang, Z. Chen, *Chem. Eng. J.* **2022**, *431*, 134224.
[52] H. Wang, C. Zhang, X. Ji, J. Yang, Z. Zhang, Y. Ma, Z. Zhang, B. Zhou, J. Shen, A. Du, *ACS Appl. Mater. Interfaces* **2022**, *14*, 10257.